Journal of Vacuum Science and Technology A

RESEARCH ARTICLE | JUNE 25 2026

Saturation behavior in a bubbler-based vapor delivery system

Rens Kamphorst ; Matijn Palings ; Evert C. Wagner ; J. Ruud van Ommen

J. Vac. Sci. Technol. A 44, 043411 (2026)
https://doi.org/10.1116/6.0005484

JVST A
Journal of Vacuum Science & Technology A

ARTICLE

pubs.aip.org/avs/jva

Saturation behavior in a bubbler-based vapor delivery system

Cite as: J. Vac. Sci. Technol. A 44, 043411 (2026); doi: 10.1116/6.0005484
Submitted: 25 March 2026 · Accepted: 8 June 2026 ·
Published Online: 25 June 2026

Rens Kamphorst,[a] Matijn Palings, Evert C. Wagner, and J. Ruud van Ommen

AFFILIATIONS

Product and Process Engineering, Delft University of Technology, Delft 2629HZ, The Netherlands

[a]**Electronic mail:** R.Kamphorst@TUDelft.nl

ABSTRACT

Bubbler-based vaporizers are widely used for chemical delivery in thin-film deposition processes, yet the mechanisms governing outlet saturation remain mostly unexplored. In this work, dry N_2 gas was bubbled through water in a stainless-steel bubbler at atmospheric pressure. Saturation of the outlet stream was tested as a function of inlet gas flow rate and vessel fill level. Using fast x-ray imaging, distinct bubble and coalescence regimes across operating conditions were identified. Despite these differences in bubble dynamics, outlet measurements showed near-complete saturation across all tested conditions. A simplified mass-transfer model indicated that exchange across bubble–liquid interfaces alone cannot account for the observed results. Instead, mass transfer at the liquid–headspace interface, enhanced by surface agitation and droplet entrainment, provides a substantial additional source for mass exchange. These findings highlight the importance of non-bubble interfaces in bubbler operation and suggest that models neglecting these effects may underestimate outlet concentrations.

I. INTRODUCTION

Bubbler-based vaporizers are used as a means by which to deliver chemicals in various processes, in particular, those related to thin-film deposition such as chemical vapor deposition (CVD), and its subclass atomic layer deposition (ALD).[1,2] Both are often employed at near-vacuum, but may be utilized under atmospheric conditions as well. For example, atmospheric pressure CVD is widely applied to alter the reflective properties of glass[3,4] and atmospheric pressure ALD may be utilized when coating granular materials.[5] In thin-film deposition systems, the bubbler serves to deliver a chemical, which is typically supplied as a liquid, to a reactor chamber in the vapor phase. This is done by introducing a carrier gas at the bottom of the vessel containing the liquid chemical via a diptube. As the formed bubbles rise through the liquid, they saturate, producing an outlet stream containing the desired chemical in the vapor phase. The outlet composition of this stream is expected to depend on, among other conditions, the used gas flow rate and the fill level of the bubbler, as both affect the residence time of the bubble within the liquid.

Both CVD and ALD are commonly performed under (low) vacuum conditions. Therefore, most studies examining bubblers did so at reduced pressures.[6,7] As saturation concentrations are highly dependent on system pressure, applicability of these studies to our system is limited, as we operate under atmospheric pressure. However, some studies reported effects of evaporative cooling during the bubbler operation,[7–9] which affects outcomes regardless of system pressure. At atmospheric pressure and a constant bubbler fill level, Maury *et al.* found the evaporated amounts of chemical to increase proportionally with inlet gas flow, until droplet entrainment occurred at high flow rates.[10]

A full understanding of the vapor delivery system requires insight into the bubble dynamics within the system. For the types of bubblers applied in thin-film deposition, these dynamics remain unexplored. Some earlier works exist on bubblers with an upward facing nozzle, in which relations between bubble viscidity and Reynolds number and bubble formation were established.[11,12] For bubbles rising in bulk liquid many prior work exists, where the ones focused on void fraction are most relevant for our work.[13–15] Furthermore, the nature of employed chemicals and the process of thin-film deposition often calls for durable bubbler vessel materials. Therefore, bubblers we consider are typically made of stainless steel, complicating bubble dynamic studies.

Despite the widespread application of bubbler systems, the operating range within which full saturation of outlet gas is obtained remains unexplored in the literature.

In this work, we characterized the bubbler performance, focusing on outlet stream, as a function of water fill level and inlet N_2 flow rate. Fast x-ray imaging was used to visualize the bubble dynamics within the bubbler vessel. This enabled the identification of distinct bubble and coalescence behavior. Furthermore, outlet vapor concentrations were measured across all experimental combinations of inlet gas flow rate and fill level. Finally, comparing these combined results to a simple model, we show that direct transport of chemicals from the liquid to the bubble within the bulk liquid is possibly not the only driver of mass transport within the bubbler system.

II. METHODS

A. Bubbler

The bubbler used for the study, displayed in Fig. 1 is a 150 ml stainless steel vessel produced by Strem Chemicals. The inlet extends into the bubbler, forming the diptube with an opening at the bottom of the vessel. Introduced gas bubbles through the liquid contained within the bubbler from the diptube outlet. As this is located in the bottom of the vessel, bubble residence time is maximized for optimal liquid–gas mass transfer. Upon breaching the liquid surface, the gas enters the headspace of the vessel, which is assumed to be well-mixed.

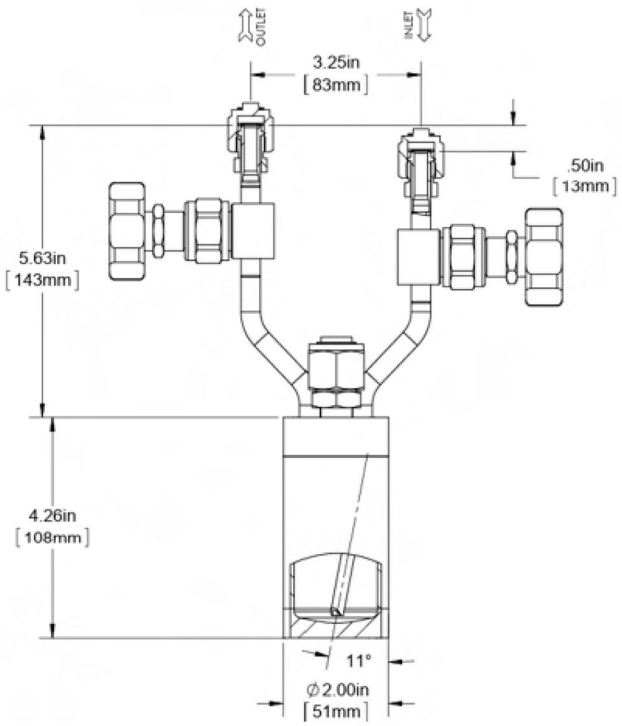

FIG. 1. Schematic image of the stainless steel bubbler used in this study.

B. X-ray imaging

To study the bubble flow regimes within the bubbler, we employed fast x-ray imaging. This technique has been shown to provide insight into opaque systems without alternating their dynamics.[16,17] The x-ray measurement principle is based on the attenuation of the rays as they pass through the object of interest, following the Lambert–Beer law, Eq. (1),

$$I(x) = I_0 e^{-\mu x}, \tag{1}$$

where $I(x)$ is the x-ray intensity measured on the detector, I_0 is the energy emitted by the x-ray source, μ is the attenuation coefficient, and x is the traversed distance through the object of interest.

To compute bubble holdup within the system, a two-point calibration was performed, requiring x-ray images of an empty bubbler and one fully filled with water. Using the reference frames of an empty and full bubbler, a void fraction between source and detector can be calculated as

$$\varepsilon = \frac{\ln(I_m/I_{full})}{\ln(I_{empty}/I_{full})}, \tag{2}$$

where ε denotes the computed relative void fraction and I_m, I_{full}, and I_{empty} correspond to the detected intensities during the measurement, measuring a full bubbler and measuring an empty bubbler, respectively.

The employed setup consists of an x-ray source (Yxlon International GmbH), which was operated in a cone beam mode, at a voltage of 150 keV, and an anode current of 8.6 mA. Opposite from the source, a two-dimensional scintillation detector (Teledyne Dalsa Xineos) was located. Detector pixel sizes are $198 \times 198\,\mu$m and a viewing area of 350×708 pixels was used in this study. As a conical x-ray beam was used, images get magnified, therefore, captured pixels effectively correspond to $143 \times 143\,\mu$m in the measurement plane. To adequately capture the dynamics of the system, images were acquired at a frame rate of 100 Hz, with an exposure time of 10 ms. The bubbler was positioned in the vertical center of the x-ray source. Dry nitrogen gas was introduced by a Bronkhorst FLOW-BUS mass flow controller with a maximum capacity of 5 l/min (STP). Bubbler fill levels were varied from 15 to 150 ml and gas flow rates were varied from 0.2 to 2.0 l/min, both in 10 equal steps, for a total of 100 experiments. Thresholding was used for binarization of the acquired x-ray images which allowed for differentiation of the bubble and liquid phases. Bubble sizes could then be calculated from the circle-equivalent projected area. Additional information on image processing and determination of bubble sizes are provided in the supplementary material.

C. Humidity measurements

To measure the relative humidity of the gas leaving the bubbler, a Rotronic HC2A-S temperature-humidity sensor (RH

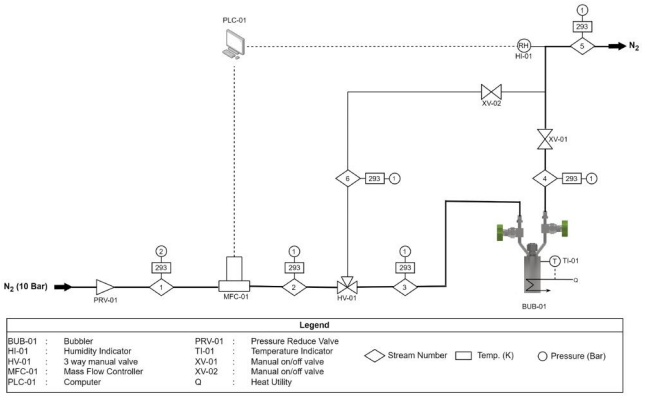

FIG. 2. Overview of the setup used to perform measurements of the outlet concentrations of the bubbler under various operating conditions.

$\pm 0.8\%$, $T \pm 0.1$ K) was used. These measurements were performed independently from x-ray imaging. As discussed in the introduction, evaporative cooling may affect bubbler outlet concentrations over time. Furthermore, thin-film deposition is typically performed at elevated temperatures, where the bubbler is temperature-controlled. Thus, to most accurately reflect the operation conditions, our bubbler was submerged in a temperature-controlled stirred waterbath at 20 °C with a volume of 5 l at all times. Measurements indicated a stable operating temperature during experiments. An overview of the system is displayed in Fig. 2. The headspace within the bubbler may saturate between experiments. Therefore, after changing an experimental setting, the system was given a minimum of 20 min to equilibrate before measurements were taken. Furthermore, the sensor itself was flushed with dry nitrogen before every measurement. The system outlet pressure was always equal to ambient pressure, upstream pressure being equal to ambient plus pressure drop, which are provided in the supplementary material. The maximum overpressure, at highest flow rate and bubbler fill level, was found to be 13.4 hPa, approximately 1.3% of the total pressure.

III. RESULTS AND DISCUSSION

A. X-ray imaging

The obtained x-ray images provided insight into the bubble dynamics within the bubbler. In Fig. 3, some representative types of bubble behavior are shown. As can be seen, the two-point calibration allowed for high contrast between the liquid and gas phase within the system. The color in the image represents the relative void fraction as calculated in Eq. (2), where 1 denotes the gas phase and 0 corresponds to the liquid. While mostly calibrated out of the images, the diptube remains somewhat visible in the liquid phase, extending to the bottom of the vessel. The top row of Fig. 3 shows typical single bubble flow, where individual bubbles form at the orifice and do not interact with one another during their ascent. This type of bubble formation is well-known in literature and sometimes referred to as static,[12,18] or period 1.[19] At higher

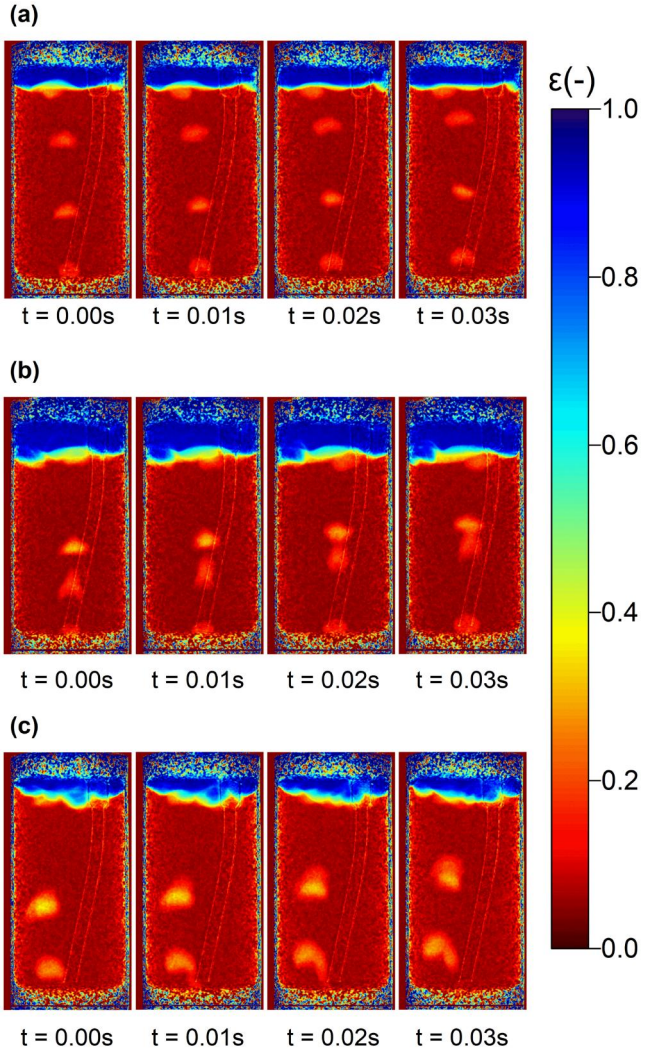

FIG. 3. X-ray images of N_2 bubbling through water in the bubbler. (a) discrete bubbling (0.2 l/min), (b) coalescence in bulk (0.4 l/min), and (c) coalescence at orifice (0.6 l/min). The color bar indicates the void fraction, ε, obtained from Eq. (2).

gas flow rates, coalescence occurs, where two types are distinguished. First of all, shown in the middle row of Fig. 3, bubbles may coalesce in the bulk liquid. This typically occurs alternately, where a bubble leaves the orifice and starts rising while the next one is formed. Due to the wake-induced flow field caused by the first bubble, the second one rises faster. This allows for the successive bubble to catch up with the one preceding it in the liquid bulk. After coalescence, the merged bubble continues to rise to the liquid surface. Subsequently, a new "first" bubble forms and starts rising, to be overtaken by again the next bubble, and so on. Every bubble rising through the bulk liquid produces a wake-induced flow field. At lower inlet gas flow rates, it takes longer for bubbles

to reach a size where buoyancy-induced detachment from the diptube occurs. This increases the gap between sequential bubbles at lower flow rates. In addition to having to traverse more distance, this gap also mitigates the magnitude of the pull experienced by the sequential bubble. Therefore, at low flow rates, the first bubble reaches the liquid surface before the next one could catch up to it. The bottom row in Fig. 3 shows a third distinct behavior: coalescence directly at the orifice, only observed at high gas flow rates. Here, initial bubble growth at the orifice exceeds the rise velocity of the preceding bubble. As a result, a bubble detaches, but is almost immediately overtaken by the next bubble, before the latter itself has detached.

A regime map was produced based on all experimental settings, showing bubble behavior for each combination of bubbler liquid volume and gas flow rate, displayed in Fig. 4. First of all it can be seen that at very low liquid volumes (<30 ml), no bubbles are observed at all. This is due to bubbles reaching the liquid surface prior to detachment from the orifice, rendering adequate bubble detection redundant. At moderate flow rates (<0.6 l/min) single bubble flow is observed along with coalescence in bulk at higher liquid volumes, which is in line with the prior discussion on bulk coalescence. At higher flow rates, coalescence shifts to the orifice at liquid volumes up to 90 ml. At higher liquid volumes, the system becomes more chaotic; no longer showing a single type of coalescence, and some bubbles undergoing multiple coalescence events. Collectively, Figs. 3 and 4 demonstrate that inlet gas velocity and liquid volume strongly influence the bubble regime within the system.

B. Humidity measurements

The measured relative humidities of outlet gas at tested combinations of bubbler liquid volume and gas flow rate are presented in Fig. 5. It can be seen that the outlet gas was nearly saturated under all tested conditions (note the break on the y axis). This is unexpected when considering the vast difference in bubble regimes presented in Fig. 4. It is possible that mass transfer in these cases is fast enough to ensure saturation. However, it may also be possible that the liquid-bubble transfer is not the sole driver of outlet vapor concentration, but is aided by transfer at the liqiud-headspace interface.

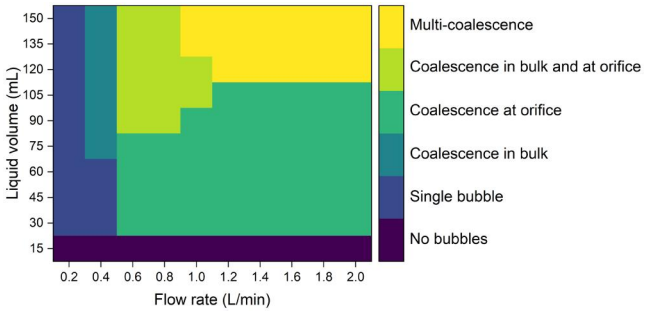

FIG. 4. Regime map displaying the bubble behavior as a function of inlet gas flow rate and bubbler liquid volume.

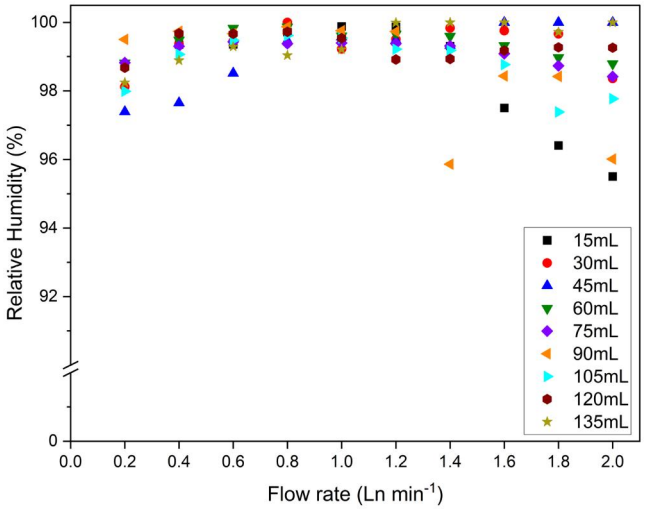

FIG. 5. Relative humidities, measured as a function of flow rate at different liquid volumes.

If bubble-liquid mass transfer were to be the sole driver, this would requires bubble saturation within the shortest bubble residence time observed in the x-ray images. To calculate whether saturation within such a time frame is expected, we considered two extreme cases for which the time to reach 95% saturation was calculated as a function of bubble radius. This percentage was chosen as all collected measurements provided in Fig. 5 exceeded this level of saturation. In the first case, we considered diffusion exclusively. This leads to the balance shown in Eq. (3), which describes diffusion inside a spherical bubble, assuming no changes in temperature and total pressure. Here, P_v denotes water vapor pressure in Pa, t corresponds to time in s, D_v is the diffusion constant in m^2/s, and r is the radial coordinate in m. The employed boundary conditions required to solve Eq. (3) are provided in Eq. (4). Here, $P_{v,sat}$ indicates the saturation vapor pressure of water and r_0 corresponds to the bubble radius, which is assumed to be constant. For any experimentally observed combination of bubble size and residence time for which saturation is predicted to occur based on this balance, it can be concluded that diffusive mass transfer alone is sufficient to achieve this saturation,

$$\frac{\partial P_v}{\partial t} = D_v\left(\frac{\partial^2 P_v}{\partial r^2} + \frac{2}{r}\frac{\partial P_v}{\partial r}\right), \tag{3}$$

$$\begin{aligned} P_v(r_0, t) &= P_{v,sat}, \\ \left.\frac{\partial P_v}{\partial r}\right|_{r=0} &= 0, \\ P_v(r, 0) &= 0. \end{aligned} \tag{4}$$

In addition, a convection-aided scenario for bubble saturation is considered. The vapor phase within bubbles is typically not static and an internal flow field increases the mass transport,

reducing the required time for saturation. Such a flow field does however require time to fully develop. For similarly sized bubbles, Li *et al.* found an establishing time of ~0.16 s.[20] The maximum internal velocity in a water-N_2 system is expected to be v =0.28 m/s.[21] Convection within rising bubbles is found in the form of two opposing circulatory motions. In our calculation, we highly simplify, neglecting a flowfield development delay and assuming convective term to be at a constant maximum velocity, always directed to the center of the bubble, Eq. (5). This overestimates mass transfer, serving as a favorable scenario for bubble saturation,

$$\frac{\partial P_v}{\partial t} = D_v\left(\frac{\partial^2 P_v}{\partial r^2} + \frac{2}{r}\frac{\partial P_v}{\partial r}\right) + v_{\max}\frac{\partial P_v}{\partial r}. \quad (5)$$

In Fig. 6, the outcomes are provided. The green region indicates combinations of bubble radii and residence times where sole diffusion is enough to result in 95% saturation. None of the experimentally observed bubbles across the 100 experimental settings fall within this region. The yellow region corresponds to radii and residence time combinations where diffusion alone does not suffice, but when a convection term is added, 95% saturation may still be reached. The majority of observed bubbles fall within this zone. Finally, the red region indicates combinations of radii and residence times where even the convection-aided mass transfer does not suffice to provide 95% saturation. It can be seen that four datapoints fall in this region. Considering that all measured samples shown in Fig. 2 were saturated beyond the cutoff of 95% used for the calculations, fast liquid-bubble mass transfer may not explain all experimental results. Both the model and experimental method assume bubbles to be spherical. From x-ray images, especially at high flow rates, this can be seen to be incorrect. As a result, surface areas are underestimated, which could explain the observed bubble saturation across all experimental conditions.

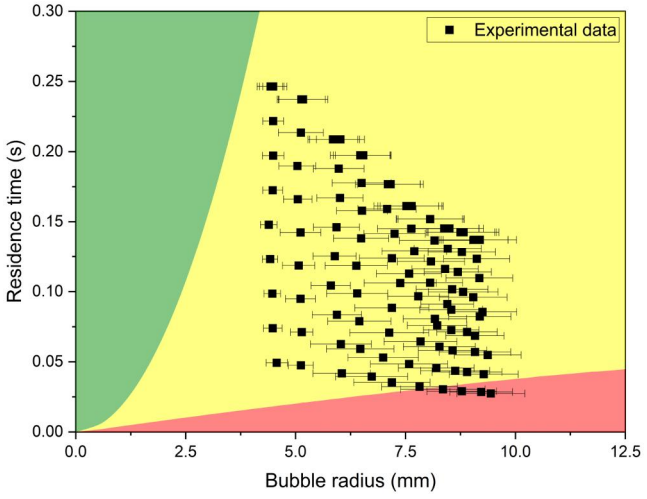

FIG. 6. Observed bubble radii and residence times within the bubbler system. Colored regions correspond to ≥95% expected saturation for green (left): diffusion only, yellow (center): diffusion and convection and red (bottom): diffusion, convection and an unaccounted for factor.

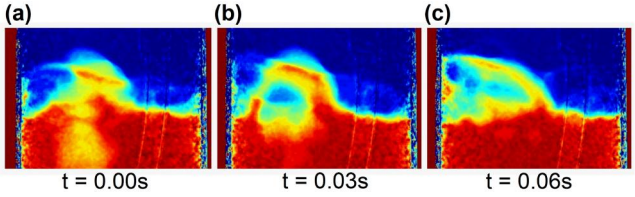

FIG. 7. X-ray images of a bubble (a) approaching the liquid-headspace interface, (b) breaching the liquid surface while remaining intact, and (c) bursting, causing agitation and droplet dispersion at the liquid surface (1.6 l/min, 120 ml).

An alternative explanation of these findings is the presence of additional sources of mass transfer, in particular, the liquid-headspace interface. The bubbles improve this transfer by constantly agitating the interface, increasing the interfacial area. This is demonstrated in Fig. 7, showcasing x-ray images of a bubble approaching the liquid surface and breaking through it. Considering the liquid-headspace interface in all subfigures, a sharp phase boundary appears to be absent, with the void fractions implying a gradient. It has to be noted that this is an artefact of the two-dimensional projection. While the true interface remains binary, the observed transition reflects an agitated surface and possible droplet entrainment. Subfigure (a) shows the agitated surface after bubble breakthrough, as well as a successive bubble approaching the liquid-headspace interface. In subfigure (b), it is shown how the bubble remains intact for a short duration of time, as a result of surface tension when reaching the liquid surface. Upon bursting, subfigure (c), it can be seen how a splash is created, introducing additional liquid-gas surface area and producing tiny droplets in the headspace which may get entrained. The extent to which either occurs increases with flow rate, however, as seen in Fig. 3, even at the lowest employed flow rate surface agitation is observed. Both surface agitation and entrainment appear to be mostly independent of bubbler liquid volume. Therefore, these additional sources of mass transfer may mitigate fill level dependency on outlet concentrations.

IV. CONCLUSIONS

In this work, we examined the dependence of bubbler outlet concentrations on inlet gas flow rate and bubbler fill level. Fast x-ray imaging showed that distinct bubble regimes emerge as a function of these operating conditions. Observed regimes included single-bubble flow, bulk coalescence, and coalescence directly at the orifice. Despite these differences in bubble dynamics, measurements of N_2 bubbled through water showed near-complete saturation at the bubbler outlet across all tested combinations of fill level and inlet gas flow rate. Through simple modeling, it was demonstrated that bubble-liquid mass transfer alone may not account for the obtained saturation, even with an optimistic approach to internal bubble convection. It was, therefore, suggested that additional sources of mass-transfer must contribute to the saturation of

outlet gas. Transfer at the liquid-headspace interface, magnified by agitation due to the bubbling, as well as droplet entrainment upon bubble bursting provide plausible mechanisms. Both enhance saturation and mitigate dependency on fill level and inlet gas flow rate. These findings indicate that bubble-liquid transfer may not be the sole driver of outlet vapor concentrations in these systems. Therefore, modeling approaches that neglect liquid-headspace interface effects may underestimate mass transfer rates. Furthermore, the results suggest that enhancing interfacial agitation, through geometry or external forcing, could lead to improved outlet concentration robustness of bubbler-based systems. As quantitative results depend strongly on gas–liquid properties, the generalizability of the presented findings to other precursor systems is limited. In particular, differences in Schmidt number, liquid viscosity, and surface tension are expected to affect mass transfer, bubble shape, and residence time. Future studies may aim to further quantify these effects.

SUPPLEMENTARY MATERIAL

Additional information on x-ray image processing, bubble size determination, and system pressure drops is given in the supplementary material.

AUTHOR DECLARATIONS

Conflict of Interest

The authors have no conflicts to disclose.

Author Contributions

R.K. and M.P. have contributed equally to this work.

Rens Kamphorst: Conceptualization (equal); Formal analysis (equal); Investigation (equal); Methodology (equal); Project administration (equal); Resources (equal); Validation (equal); Writing – original draft (equal). **Matijn Palings:** Data curation (equal); Formal analysis (equal); Investigation (equal); Methodology (equal); Visualization (equal); Writing – original draft (equal). **Evert C. Wagner:** Investigation (equal); Methodology (equal); Writing – review & editing (equal). **J. Ruud van Ommen:** Conceptualization (equal); Funding acquisition (equal); Resources (equal); Writing – review & editing (equal).

DATA AVAILABILITY

Data are made publicly accessible through the 4TU repository.

REFERENCES

[1]D. Bour, Z. Yang, and C. Chua, J. Cryst. Growth **310**, 2673 (2008).
[2]R. Kamphorst, P. Wanjari, S. Saedy, J. F. van Dam, A. Thijssen, P. Brüner, T. Grehl, G. M. Meesters, and J. R. van Ommen, Surf. Interfaces **45**, 103852 (2024).
[3]E. R. Klobukowski, W. E. Tenhaeff, J. W. McCamy, C. S. Harris, and C. K. Narula, J. Mater. Chem. C **1**, 6188 (2013).
[4]G. A. Neuman, J. Non-Cryst. Solids **218**, 92 (1997).
[5]P. Piechulla, M. Chen, A. Goulas, R. Puurunen, and J. R. Van Ommen, Chem. Mater. **38**, 20 (2026).
[6]S. D. Hersee and J. M. Ballingall, J. Vac. Sci. Technol. A **8**, 800 (1990).
[7]A. Love, S. Middleman, and A. K. Hochberg, J. Cryst. Growth **129**, 119 (1993).
[8]S. Middleman, J. Cryst. Growth **114**, 13 (1991).
[9]J. E. Maslar, W. A. Kimes, B. A. Sperling, and R. K. Kanjolia, J. Vac. Sci. Technol. A **37**, 041506 (2019).
[10]F. Maury, F.-D. Duminica, and F. Senocq, Chem. Vap. Depos. **13**, 638 (2007).
[11]S. Ramakrishnan, R. Kumar, and N. Kuloor, Chem. Eng. Sci. **24**, 731 (1969).
[12]J. Davidson and B. Schueler, Trans. Inst. Chem. Eng. **38**, 335 (1960).
[13]K. Mishima and M. Ishii, "Flow regime transition criteria consistent with two-fluid model for vertical two-phase flow," Technical Report (Argonne National Laboratory, IL, 1983) [PWR].
[14]K. Mishima and M. Ishii, Int. J. Heat Mass Transfer **27**, 723 (1984).
[15]K. Mishima and T. Hibiki, Int. J. Multiphase Flow **22**, 703 (1996).
[16]G. Bruni, R. Solimene, A. Marzocchella, P. Salatino, J. Yates, P. Lettieri, and M. Fiorentino, Powder Technol. **128**, 11 (2002).
[17]R. Kamphorst, P. C. van der Sande, K. Wu, E. C. Wagner, M. K. David, G. M. H. Meesters, and J. R. van Ommen, KONA Powder Part. J. **41**, 254 (2023).
[18]H. Tsuge, P. Rüdin, and R. Kammel, J. Chem. Eng. Jpn. **19**, 326 (1986).
[19]V. K. Badam, V. Buwa, and F. Durst, Can. J. Chem. Eng. **85**, 257 (2007).
[20]X. Li, G. Chen, P. Zhang, W. Wang, and J. Li, Phys. Fluids **31**, 117107 (2019).
[21]M. R. Ansari and M. E. Nimvari, Ann. Nucl. Energy **38**, 2770 (2011).